Materials Advances

ROYAL SOCIETY OF CHEMISTRY

PAPER

View Article Online
View Journal | View Issue

Cite this: *Mater. Adv.*, 2025, 6, 9043

The core–shell structure improving the third-order nonlinear optical response of Zintl ions: $M@Sn_9^{4-}$

Jiali Chen,[abcd] Zirui Wang,[ad] Yayu Yan,[acd] Wanting Xia,[abcd] Xiaolan Zheng,[acd] Qiao-hong Li *[acde] and Jian Zhang *[acd]

The core–shell structure significantly impacts multiple material properties, yet systematic investigations into the enhancement of third-order nonlinear optical properties in metal-encapsulated clusters are still lacking. This paper explores the influence of the core–shell structure on enhancing the third-order nonlinear optical (NLO) properties of materials, focusing on the $M@Sn_9^{4-}$ series compounds. By employing theoretical calculations and excited-state analysis, it is revealed that the introduction of a core–shell structure effectively improves the third-order NLO performance, with specific metals as the core demonstrating superior NLO responses due to enhanced electron transfer pathways and three-dimensional aromaticity. Notably, $Pd@Sn_9^{4-}$ exhibits a superior third-order nonlinear optical response, which is an order of magnitude greater than that of Sn_9^{4-}. These findings offer a theoretical basis for optimizing third-order NLO performance in inorganic cluster systems, with potential implications for advanced optical materials development.

Received 1st September 2025,
Accepted 9th October 2025

DOI: 10.1039/d5ma00992h

rsc.li/materials-advances

Introduction

Nonlinear optics has progressively emerged since the advent of laser technology and has become one of the most dynamic research areas in modern science.[1,2] Initially, research primarily concentrated on the second-order nonlinear optical properties of crystals. A diverse range of materials, including both organic and inorganic compounds, have found widespread application.[3–6] Furthermore, with rapid advancements in optical research, third-order nonlinear optical materials have gradually gained prominence, demonstrating broad application prospects in optical switches, optical limiting, ultrafast photonics, and other fields.[7–11]

The core–shell structure exerts a significant influence on multiple properties of materials, including photocatalysis, thermal catalysis, and optical characteristics.[12,13] In particular, the incorporation of the core–shell structure plays a crucial role in enhancing third-order nonlinear optical responses. Wang Jun's research group utilized a one-step solvothermal method to synthesize MoS_2/CNT nanocomposite materials with a core–shell structure. Studies have shown that the third-order nonlinear optical properties of the composites are significantly enhanced compared to those of pure MoS_2 or carbon nanotubes.[14] In Zhu's work,[15] the core–shell structure was successfully implemented to enhance the optical limiting effect of metal-oxygen clusters through a combination of theoretical and experimental approaches. This study demonstrated that the core–shell structure serves as an effective strategy for improving the optical properties. Breakthroughs have been achieved recently in the experimental synthesis of endohedral all-metal clusters. The research group led by Zhongming Sun has successfully synthesized a series of transition-metal-embedded plumbaspherenes and stannaspherenes. In collaboration with theoretical chemists, they have conducted in-depth investigations into the stabilization mechanisms and formation pathways of these novel compounds.[16–19] In 2023, a significant milestone was reached with the successful synthesis[20] of the first all-metal fullerene cluster $[K@Au_{12}Sb_{20}]^{5-}$. Remarkable progress has been made in the study of main-group Zintl ion clusters, where d- or f-block metal atoms can be encapsulated within cage-like structures composed of p-block (semi)metals.[21,22] However, systematic investigations into the structure–property relationships regarding the enhancement of third-order nonlinear optical properties through the core–shell structure in metal-encapsulated clusters are still lacking.

[a] State Key Laboratory of Structural Chemistry, Fujian Institute of Research on the Structure of Matter, Chinese Academy of Sciences, Fuzhou 350002, China. E-mail: lqh2382@fjirsm.ac.cn, zhj@fjirsm.ac.cn
[b] College of Chemistry, Fuzhou University, Fuzhou 350108, China
[c] Fujian College, University of Chinese Academy of Sciences, Fuzhou 350002, China
[d] Chinese Academy of Sciences, University of Chinese Academy of Sciences, Beijing 100049, China
[e] Fujian Provincial Key Laboratory of Theoretical and Computational Chemistry, Xiamen 361005, China

Zintl phase compounds have garnered significant attention due to their unique electronic structure and physical–chemical properties.[23,24] These compounds typically consist of metal cations and complex nonmetallic anions, exhibiting diverse structural and performance characteristics.[25,26] Recently, $M@Sn_9^{4-}$ series compounds with a core–shell structure have been synthesized by incorporating transition metal elements into Zintl phases, thereby expanding their potential applications. These compounds not only retain the inherent stability of Zintl phases but also modulate the electronic structure through the introduction of central atoms, thus showing promising application value in catalysis, photoelectric conversion, and other fields.[27,28] In this work, we aim to thoroughly investigate structure optimization, third-order NLO performance calculation, excited-state analysis, and aromaticity analysis of $M@Sn_9^{4-}$ series compounds, providing a theoretical foundation for optimizing their third-order nonlinear optical performance and expanding their applications.

Computational details

All the calculations were performed using Gaussian 16.[29] Geometry optimization, third-order NLO properties, and excitation energy calculation were realized by DFT and time-dependent DFT (TD-DFT). The geometry optimizations and analysis of nucleus independent chemical shift (NICS),[30,31] iso chemical shielding surface (ICSS),[32,33] and adaptive natural density partitioning (AdNDP)[34] were performed using the Perdew–Burke–Ernzerhof (PBE0)[35] functional and def2SVP[36,37] basis sets with D3 dispersion correction of Grimme.[38] The static third-order nonlinear polarizability calculations were performed using the CAM-B3LYP[39] functional and def2SVPD[36] basis sets with D3 dispersion correction of Grimme. The excited-state calculations were performed using the cam-B3LYP functional and def2SVP basis sets with D3 dispersion correction of Grimme. The frequency-dependent NLO hyperpolarizabilities were calculated by the Coupled Perturbed Kohn–Sham (CPKS)[40] method. To gain a deeper understanding of the wave function, Multiwfn 3.8(dev)-code[41] and VMD software[42] were used to analyze the electronic structures, hyperpolarizability, excitation characteristics, and aromaticity.

Results and discussion

Electronic structure analysis

Zintl anions react with organic halides or organometallic complexes to form inter-metalloid and heterometallic clusters, driven by their unique electronic structures and potential applications. Binary inter-metalloid clusters of group 14 elements are synthesized by treating Zintl phases with organometallic complexes, yielding deltahedral or non-deltahedral structures. Deltahedral clusters, resembling boranes, are rationalized using Wade–Mingos rules and include 9-vertex cages[23] like $M@Sn_9^{4-}$. To investigate the core–shell structure of $M@Sn_9^{4-}$ series compounds on the third-order nonlinear optical properties in detail, we constructed a series of $M@Sn_9^{4-}$ series compounds with different cores based on the experimental $Ni@Sn_9^{4-}$ structure. The structure of $M@Sn_9^{4-}$ in Zintl compounds was investigated, with a transition metal element selected as the central atom for substitution (Fig. 1a). Through structural optimization, nine closed-shell stable configurations were obtained (M = Ti, Fe, Ni, Zr, Ru, Pd, Hf, Os, and Pt), and it was observed that the point groups of these structures changed post-optimization (Fig. 1c and Table S1). The $Ni@Sn_9^{4-}$, $Pd@Sn_9^{4-}$, and $Pt@Sn_9^{4-}$ induce

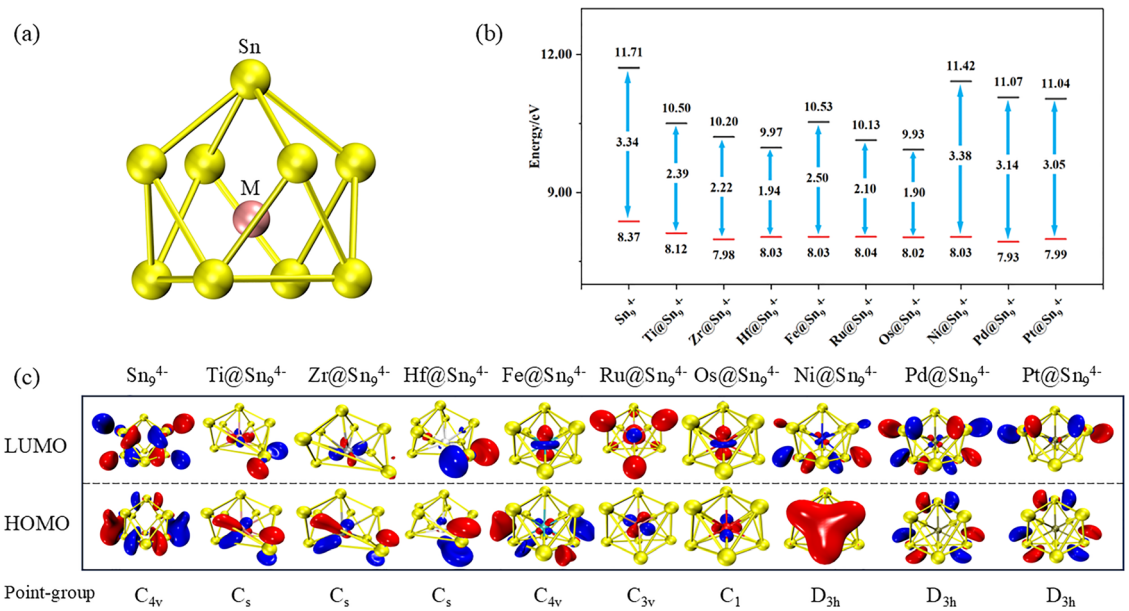

Fig. 1 (a) The structure of $M@Sn_9^{4-}$ (M = Ti, Fe, Ni, Zr, Ru, Pd, Hf, Os, and Pt) in Zintl compounds. (b) The HOMO, LUMO, and HOMO–LUMO energy gap values of the Sn_9^{4-} shell and the nine $M@Sn_9^{4-}$ structures. (c) The configurations, HOMO, LUMO, and point groups of the Sn_9^{4-} shell and the nine $M@Sn_9^{4-}$ structures.

a transformation from the original C_{4v} configuration of $Sn@Sn_9^{4-}$ to a higher-symmetry D_{3h} configuration, while $Fe@Sn_9^{4-}$ retains the C_{4v} configuration of Sn_9^{4-}. Meanwhile, the symmetry of other structural configurations is reduced. In Fig. 1b and c, the highest occupied molecular orbital (HOMO) and lowest unoccupied molecular orbital (LUMO) of the Sn_9^{4-} shell and the nine $M@Sn_9^{4-}$ structures are illustrated,[43] along with the calculated HOMO–LUMO gap which serves as a preliminary indicator for the electronic excitation energy. It has been observed that clusters with a small HOMO–LUMO energy gap possess good third-order NLO properties,[44–47] thus tuning this gap is also a strategy we have focused on. From Fig. 1b, it is evident that the introduction of the central atom significantly affects the frontier molecular orbitals of $M@Sn_9^{4-}$, leading to varying degrees of decrease in both HOMO and LUMO energies, with a more pronounced effect on the LUMO. Comparative analysis reveals that except for $Ni@Sn_9^{4-}$, all $M@Sn_9^{4-}$ clusters exhibit reduced energy gaps relative to the Sn_9^{4-} cluster. Notably, the most significant reduction is observed in $Os@Sn_9^{4-}$, which demonstrates a remarkably narrow energy gap of 1.90 eV. Table 1 lists the natural population analysis (NPA) charges for ten structures, including the net charge of the central atom M, the range of net charge variation for the shell atoms Sn, and the difference in charge variation. Notably, the introduced central atom can function either as positive or negative charge centers. For instance, the central atom in $Ti@Sn_9^{4-}$ and $Hf@Sn_9^{4-}$ exhibits positive charge center behavior (0.19, 0.18), whereas the others in $Pd@Sn_9^{4-}$ and $Pt@Sn_9^{4-}$ serve as negative charge centers (−1.13, −1.29). This phenomenon may be attributed to differences in electronegativity. Ti, Zr, and Hf tend to lose electrons more readily compared to Sn, while Ru, Os, Pd, and Pt gain electrons from Sn more easily (Fig. S1). These findings highlight the significant influence of central metal atoms on the structural symmetry, electronic properties, and charge distribution of $M@Sn_9^{4-}$ clusters, providing a foundation for further exploration of their third-order nonlinear optical responses and the design of advanced functional materials.

Third-order nonlinear optical properties

It was found that the introduction of a core–shell structure in an inorganic–organic cluster system effectively improved the third-order nonlinear optical properties of compounds in the previous cooperation.[14,15] Our research focuses on the influence of metal–metal interactions on third-order nonlinear optical properties, with particular emphasis on metallic aromatic systems, which have demonstrated exceptional third-order nonlinear optical performance.[48] Our findings reveal that cyclic Sn_4 clusters exhibit superior performance due to metallic aromaticity compared to their linear and conical counterparts. Herein, we place significant emphasis on investigating the applicability of this phenomenon in purely inorganic cluster systems. To further elucidate the relationship between core–shell structures and third-order nonlinear optics, we employed the coupled perturbed Kohn–Sham (CPKS) method to calculate the static third-order nonlinear polarizability (γ) for ten structures.[40] As illustrated in Fig. 2a, the introduction of a central atom into the Sn_9^{4-} shell results in an increase in the third-order nonlinear polarizability, indicating that the implementation of a core–shell structure in inorganic systems is advantageous for enhancing third-order nonlinear optical properties. Notably, the third-order optical properties exhibit an improving trend as the group number of the elements increases. Table S2 compares the γ_{tot} values of Sn_9^{4-} (4.93×10^5): $Ni@Sn_9^{4-}$ (1.12×10^6), $Pd@Sn_9^{4-}$ (1.17×10^6), and $Pt@Sn_9^{4-}$ (9.74×10^5) for the 10th group elements; $Fe@Sn_9^{4-}$ (1.05×10^6), $Ru@Sn_9^{4-}$ (8.66×10^5), and $Os@Sn_9^{4-}$ (7.94×10^5) for the 8th group elements; and $Ti@Sn_9^{4-}$ (5.83×10^5), $Zr@Sn_9^{4-}$ (6.49×10^5), and $Hf@Sn_9^{4-}$ (6.63×10^5) for the 4th group elements. These numerical results further demonstrate

Table 1 The NPA charges for the Sn_9^{4-} shell and the nine $M@Sn_9^{4-}$ structures. Δ charge (Sn) refers to the charge difference (max−min) among the Sn atoms

	Net charge (M)	Net charge (Sn)	Δ charge (Sn)
Sn_9^{4-}	—	−0.57 to −0.37	0.20
$Ti@Sn_9^{4-}$	0.19	−0.74 to −0.35	0.39
$Zr@Sn_9^{4-}$	−0.16	−0.67 to −0.29	0.38
$Hf@Sn_9^{4-}$	0.18	−0.73 to −0.32	0.41
$Fe@Sn_9^{4-}$	−0.18	−0.55 to −0.37	0.18
$Ru@Sn_9^{4-}$	−0.67	−0.46 to −0.32	0.14
$Os@Sn_9^{4-}$	−0.72	−0.45 to −0.28	0.17
$Ni@Sn_9^{4-}$	−0.16	−0.40 to −0.49	0.09
$Pd@Sn_9^{4-}$	−1.13	−0.42 to −0.27	0.15
$Pt@Sn_9^{4-}$	−1.29	−0.39 to −0.25	0.14

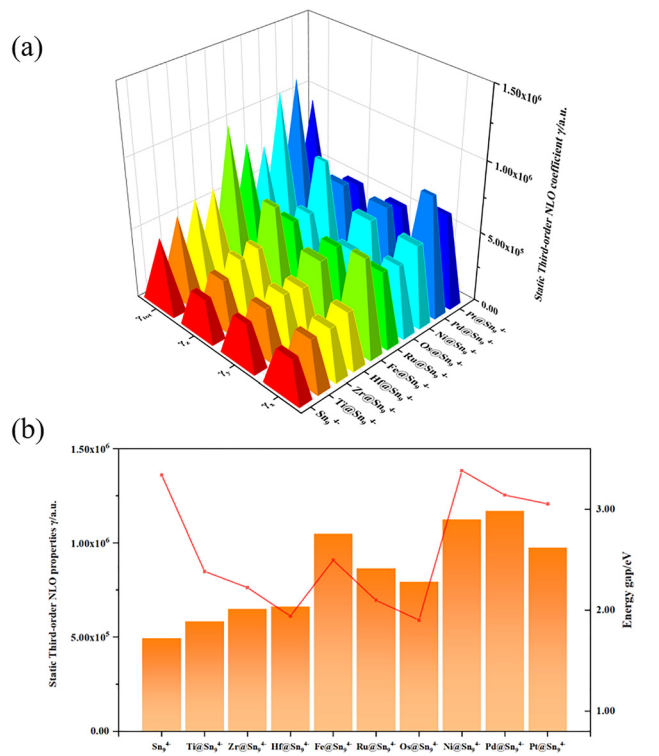

Fig. 2 (a) The static third-order nonlinear polarizability (γ) for the Sn_9^{4-} shell and the nine $M@Sn_9^{4-}$ structures. (b) The relationship between E_{gap} and third-order coefficient (γ_{tot}).

the correlation between the central metal atoms' group number and the enhancement of the third-order optical properties.

In the original inorganic–organic system, a smaller HOMO–LUMO energy gap is often empirically associated with larger third-order nonlinear optical coefficients, making energy gap engineering a common strategy for enhancing performance.[44–47] The denominator of the polarizability expression includes excitation energy, which is related to the energy difference between the two orbitals that dominate electron excitation. Generally, a smaller E_{gap} indicates a smaller energy difference between occupied and unoccupied orbitals, leading to lower excitation energy and higher polarizability. In the case of the M@Sn_9^{4-} series Zintl structures, the correlation between the HOMO–LUMO energy gap and the third-order polarizability (γ) is weak (Fig. 2b). This indicates that for these Zintl clusters, other factors, such as structural symmetry and the specific nature of the central metal atom, play a more dominant role in determining their NLO performance than the HOMO–LUMO gap alone. According to previous analyses, there is a strong correlation between polarizability and the symmetry of the structural point group. Structures with higher point group symmetry (D_{3h}), such as Ni@Sn_9^{4-}, Pd@Sn_9^{4-}, and Pt@Sn_9^{4-}, exhibit superior performance in third-order nonlinear optical responses. These results demonstrate that the core–shell structure improves the third-order nonlinear optical response of Sn_9^{4-}. The enhancement of third-order nonlinear optical properties in M@Sn_9^{4-} clusters is predominantly governed by structural symmetry and the choice of central metal atoms, rather than energy gap engineering, highlighting the unique potential of purely inorganic core–shell systems for advanced optical applications.

Analysis of excited states

Electronic excitation research is a pivotal area within quantum chemistry, encompassing the study of electronic transitions between energy levels and the mechanisms by which these transitions influence the properties of materials. Through the analysis of the excited state properties of the structure, it is observed that the introduction of the central atom generally results in a redshift of the ultraviolet absorption wavelength (Fig. 3a), which aligns with previous research findings.[48] Although the molar absorption coefficient of M@Sn_9^{4-} compounds is generally lower than that of Sn_9^{4-}, Pd@Sn_9^{4-} exhibits the best third-order nonlinear optical response, along with a more intense UV-Vis absorption profile than its analogues (Fig. 3a). It is hypothesized that the presence of the central atom may introduce an increased steric hindrance within the shell structure, thereby impeding the penetration of ultraviolet light and consequently reducing its absorption efficiency. This phenomenon has been documented in the literature, where bimetallic MOFs with different metal ions show enhanced third-order NLO properties, but the UV absorption efficiency remains unaffected due to steric hindrance.[49]

We concentrate on Pd@Sn_9^{4-}, which exhibits superior third-order performance compared to other M@Sn_9^{4-} compounds. By analyzing the orbital transitions between Sn_9^{4-} and Pd@Sn_9^{4-} (as illustrated in Fig. 3b–e), it is evident that significant metal conjugation is involved in the electron transfer

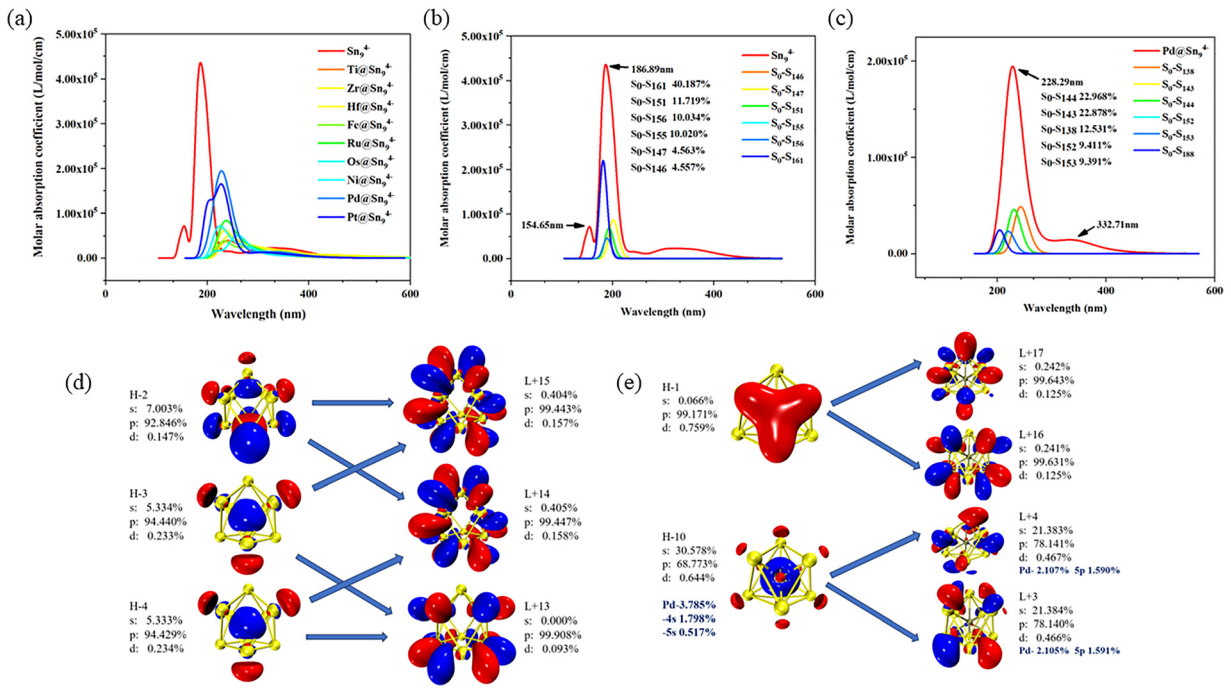

Fig. 3 (a) Normalized UV-vis absorption of the Sn_9^{4-} shell and the nine M@Sn_9^{4-} structures. (b) Normalized UV-vis absorption and emission spectra of Sn_9^{4-}. (c) Normalized UV-vis absorption and emission spectra of Pd@Sn_9^{4-}. (d) The major orbital transition of Sn_9^{4-}. (e) The major orbital transition of Pd@Sn_9^{4-}.

process. It is important to distinguish between the first excited state (S_1), which defines the HOMO–LUMO energy gap (E_{gap}), and the states responsible for this intense absorption feature. Our analysis focuses on the latter, as transitions with high oscillator strength are major contributors to the nonlinear optical response. Detailed orbital transition data are provided in Tables S4 and S5. The characteristic peak of Sn_9^{4-} is located at 186.89 nm, with a contribution of 40.19% attributed to the excited state S_0–S_{141}. Among the excited states contributing to the characteristic peak, the predominant orbital transitions include HOMO−2 (H−2) → LUMO+15 (L+15), HOMO−2 (H−2) → LUMO+14 (L+14), HOMO−3 (H−3) → LUMO+15 (L+15), HOMO−3 (H−3) → LUMO+13 (L+13), HOMO−4 (H−4) → LUMO+14 (L+14), and HOMO−4 (H−4) → LUMO+13 (L+13). Notably, the primary components of these orbitals are p-orbitals, implying that the p-orbitals of Sn atoms are predominantly involved in the excitation process. The characteristic peak of $Pd@Sn_9^{4-}$ is observed at 228.29 nm, with contributions of 22.99% and 22.88% from the excited states S_0–S_{144} and S_0–S_{143}, respectively. In the case of $Pd@Sn_9^{4-}$, the dominant orbital transitions are H−1 → L+17, H−1 → L+16, H−10 → L+4, and H−10 → L+3, with Pd contributing to the composition of the H−10, L+4, and L+3 orbital components. In $Pd@Sn_9^{4-}$, not only does the Sn shell participate in electron transfer, but the Pd core also plays an important role, thereby enriching the electron transfer pathways and enhancing the third-order performance of the structure. The same phenomenon is observed in other $M@Sn_9^{4-}$ compounds.

To gain a deeper understanding of the molecular structure and electron excitation modes, the electron–hole distribution elucidates the conditions of electrons and holes corresponding to different excited states (Fig. 4 and Table S6).[41,50,51] A higher electron–hole overlap Sr (with an upper limit of 1.0) indicates that the distribution characteristics of holes and electrons in $Pd@Sn_9^{4-}$ are nearly identical. Among the five primary excited states corresponding to the characteristic peaks of $Pd@Sn_9^{4-}$, the values of Sr range from 0.815 a.u. (S_0–S_{152}) to 0.870 a.u. (S_0–S_{138}). Conversely, a smaller hole–electron separation t (significantly less than 0) suggests that the holes and electrons in $Pd@Sn_9^{4-}$ are not substantially separated. Across these five primary excited states, the values of t range from −2.016 Å (S_0–S_{138}) to −1.532 Å (S_0–S_{152}). Specifically, holes are predominantly located in the Sn_9^{4-} shell region, while both the core and shell contribute to the distribution of holes and electrons (Fig. S2). Further interfragment charge transfer (IFCT) analysis (Table S7) confirmed a bidirectional electron transfer between the Pd core and the Sn_9^{4-} shell, involving both charge transfer (CT) and local excitation (LE).[41,52] As a result of this transfer, the Pd core acquires electrons from the Sn_9^{4-} shell. In summary, electronic excitation research within quantum chemistry reveals that the introduction of a central atom in $M@Sn_9^{4-}$ compounds influences the ultraviolet absorption properties, often resulting in a redshift. Among these compounds, $Pd@Sn_9^{4-}$ exhibits superior third-order nonlinear optical performance, with its electronic transitions involving significant metal conjugation and contributions from both the Sn shell and Pd core. Detailed orbital transition analysis and electron–hole distribution studies elucidate the complex electron transfer pathways and interaction mechanisms, confirming bidirectional charge transfer between the core and shell, thereby enriching the understanding of electronic excitations in such structures.

(a)

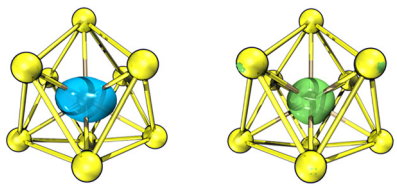

(b)

$Pd@Sn_9^{4-}$	core			shell			heatmap
	Hole	Electron	Overlap	Hole	Electron	Overlap	
S_0-S_{138}	19.41%	32.21%	25.01%	80.59%	67.79%	73.91%	
S_0-S_{143}	16.07%	41.83%	25.92%	83.93%	58.17%	69.88%	
S_0-S_{144}	16.10%	41.71%	25.91%	83.90%	58.29%	69.94%	
S_0-S_{152}	9.26%	57.82%	23.13%	90.74%	42.18%	61.87%	
S_0-S_{153}	9.24%	58.17%	23.18%	90.76%	41.83%	61.62%	

Fig. 4 (a) The centers of electron–hole in $Pd@Sn_9^{4-}$. (b) Composition of electron–hole in $Pd@Sn_9^{4-}$ core–shell structure.

Aromatic analysis

Nuclear independent chemical shift (NICS) is a widely used measure of aromaticity,[30,31] and the shielding value in aromatic systems is usually positive, that is, NICS is negative. The ring current generated in the conjugated rings in the aromatic system generates an induced magnetic field, which shields the external magnetic field to some extent. $NICS(1)_{zz}$ refers to the negative value of the shielding tensor component perpendicular to the ring plane direction 1 Å. $NICS(1)_{zz}$ mainly measures π aromaticity. By comparing the NICS values of each Sn_9^{4-} shell and $Pd@Sn_9^{4-}$ in Fig. 5a and b, $NICS(1)_{zz}$ are −65.88 ppm and −137.50 ppm. This comparison reveals that the $NICS(1)_{zz}$ value becomes significantly more negative upon the introduction of the central Pd atom, indicating that the $Pd@Sn_9^{4-}$ system possesses enhanced aromaticity compared to the Sn_9^{4-} shell. This conclusion is also applicable to other $M@Sn_9^{4-}$ systems (Table S8). After the introduction of the central atom, the surface of the increased central atom has a negative NICS value, which increases the aromaticity of the whole structure. Iso-chemical shielding surfaces (ICSS) is a method to study NICS on a three-dimensional level, ICSS principle is the same as NICS principle, and $ICSS_{zz}$ is equivalent to $NICS_{zz}$ iso-surface.[32,50] The prominent green isosurface in Fig. 5b indicates that there is a strong magnetic shielding effect in the internal region of the structure, which enables the freely moving π electrons to generate magnetic induction ring currents within the structure that offset the external magnetic field, thus further confirming the aromatics. Electron localization function

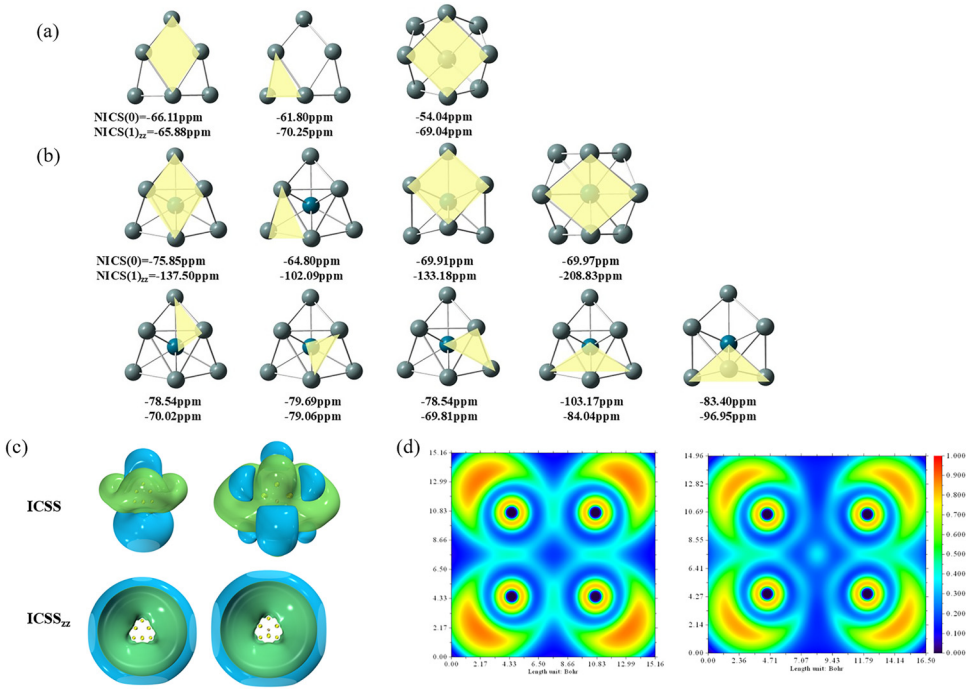

Fig. 5 (a) NICS(0) and NICS(1)$_{zz}$ of the Sn_9^{4-} shell. (b) NICS(0) and NICS(1)$_{zz}$ of $Pd@Sn_9^{4-}$. (c) ICSS and ICSS$_{zz}$ of the Sn_9^{4-} shell and $Pd@Sn_9^{4-}$. (d) ELF of the Sn_9^{4-} shell and $Pd@Sn_9^{4-}$.

(ELF) is shown in Fig. 5c, the more blue the color is, the better the delocalization is.[53–55] It can be seen that the introduction of the central atom enhances the delocalization of the electrons and weakens the bond formation between Sn–Sn to a certain extent. At the same time, adaptive natural density partitioning (AdNDP) analysis (Table S9) found that the structural bonding changes after the introduction of the central atom, the bonding modes are more diverse and the dissociation is stronger.[34] Moreover, in $Pd@Sn_9^{4-}$, more polycentric electronic bonds are formed between Pd–Sn than Sn–Sn. In summary, the consistent enhancement of aromaticity, as evidenced by NICS, ICSS, ELF, and AdNDP analyses, is identified as a contributing factor conducive to improving the third-order nonlinear optical response performance of the $M@Sn_9^{4-}$ structure.

Conclusions

In summary, we have conducted a thorough investigation into the structure optimization, calculation of third-order nonlinear optical (NLO) performance, excited-state analysis, and aromaticity analysis of the $M@Sn_9^{4-}$ series compounds. It has been demonstrated that the core–shell structure represents an effective strategy for enhancing the third-order NLO properties of Sn_9^{4-} based compounds. By investigating the $M@Sn_9^{4-}$ series, we have shown that the enhancement of these properties is predominantly governed by structural symmetry and the choice of the central metal. Notably, $Pd@Sn_9^{4-}$ exhibits a superior third-order nonlinear optical response, which is an order of magnitude greater than Sn_9^{4-}, while simultaneously maintaining a better UV-Vis spectral response compared to other $M@Sn_9^{4-}$compounds. Furthermore, the introduction of the central atom leads to a change in aromaticity, as evidenced by the NICS values, which further supports the enhancement of third-order nonlinear optical properties. These findings provide a theoretical foundation for optimizing the third-order nonlinear optical performance of inorganic cluster systems and have potential implications for the development of advanced optical materials.

Author contributions

Jiali Chen: writing – original draft, and data curation; Zirui Wang: investigation and validation; Yayu Yan, Wanting Xia and Xiaolan Zheng: data curation; Qiao-hong Li: conceptualization, supervision, writing – review & editing, funding acquisition and methodology; Jian Zhang: funding acquisition and methodology.

Conflicts of interest

There are no conflicts to declare.

Data availability

The data that support the findings of this study are available in the supplementary information (SI). The supplementary information file includes contents: computational models and supplementary figures. Supplementary information is available. See DOI: **https://doi.org/10.1039/d5ma00992h**.

Acknowledgements

This work is supported by the National Natural Science Foundation of China (22571298, U23A2095 and 92161105).

References

1 D. R. Kanis, M. A. Ratner and T. J. Marks, Design and construction of molecular assemblies with large second-order optical nonlinearities. Quantum chemical aspects, *Chem. Rev.*, 1994, **94**, 195–242.
2 J. L. Oudar and D. S. Chemla, Hyperpolarizabilities of the nitroanilines and their relations to the excited state dipole moment, *J. Chem. Phys.*, 1977, **66**, 2664–2668.
3 C. Chen, Y. Wu, A. Jiang, B. Wu, G. You, R. Li and S. Lin, New nonlinear-optical crystal: LiB_3O_5, *J. Opt. Soc. Am. B*, 1989, **6**, 616–621.
4 G. D. Boyd, R. C. Miller, K. Nassau, W. L. Bond and A. Savage, $LiNbO_3$: An efficient phase matchable nonlinear optical material, *Appl. Phys. Lett.*, 1964, **5**, 234–236.
5 W. L. Smith, KDP and ADP transmission in the vacuum ultraviolet, *Appl. Opt.*, 1977, **16**, 1798.
6 I. Tordjman, R. Masse and J. C. Guitel, Structure cristalline du monophosphate $KTiPO_5$, *Z. Kristallogr.*, 1974, **139**, 103–115.
7 J. M. Hales, J. Matichak, S. Barlow, S. Ohira, K. Yesudas, J.-L. Brédas, J. W. Perry and S. R. Marder, Design of Polymethine Dyes with Large Third-Order Optical Nonlinearities and Loss Figures of Merit, *Science*, 2010, **327**, 1485–1488.
8 S. Mukhopadhyay, C. Risko, S. R. Marder and J.-L. Brédas, Polymethine dyes for all-optical switching applications: a quantum-chemical characterization of counter-ion and aggregation effects on the third-order nonlinear optical response, *Chem. Sci.*, 2012, **3**, 3103–3112.
9 X. Liu, Q. Guo and J. Qiu, Emerging Low-Dimensional Materials for Nonlinear Optics and Ultrafast Photonics, *Adv. Mater.*, 2017, **29**, 1605886.
10 P.-A. Bouit, G. Wetzel, G. Berginc, B. Loiseaux, L. Toupet, P. Feneyrou, Y. Bretonnière, K. Kamada, O. Maury and C. Andraud, Near IR Nonlinear Absorbing Chromophores with Optical Limiting Properties at Telecommunication Wavelengths, *Chem. Mater.*, 2007, **19**, 5325–5332.
11 C. Andraud, R. Fortrie, C. Barsu, O. Stéphan, H. Chermette and P. L. Baldeck, Excitonically Coupled Oligomers and Dendrimers for Two-Photon Absorption, *Adv. Polym. Sci.*, 2008, **214**, 149–203.
12 J. Chen, L. Lin, P. Lin, L. Xiao, L. Zhang, Y. Lu and W. Su, A direct Z-scheme $Bi_2WO_6/La_2Ti_2O_7$ photocatalyst for selective reduction of CO_2 to CO, *Chin. J. Struct. Chem.*, 2023, **42**, 100010.
13 W. Tan, C. Zhang, T. Huang and B. Zhang, Recent progress of newly developed functional building units and corresponding nonlinear optical materials, *Chin. J. Struct. Chem.*, 2023, **42**, 100098.
14 X. Zhang, A. Selkirk, S. Zhang, J. Huang, Y. Li, Y. Xie, N. Dong, Y. Cui, L. Zhang, W. J. Blau and J. Wang, Inside Cover: MoS2/Carbon Nanotube Core–Shell Nanocomposites for Enhanced Nonlinear Optical Performance (Chem. Eur. J. 14/2017), *Chem. – Eur. J.*, 2017, **23**, 3223.
15 Y. Zhu, Z. Wang, D. Li, Y. D. Zhu, Q. H. Li, D. S. Li and L. Zhang, Silver-Templated γ-Keggin Alkyltin-Oxo Cluster: Electronic Structure and Optical Limiting Effect, *Angew. Chem., Int. Ed.*, 2022, **61**, e202202853.
16 C.-C. Shu, H. W. T. Morgan, L. Qiao, J. E. McGrady and Z.-M. Sun, A family of lead clusters with precious metal cores, *Nat. Commun.*, 2020, **11**, 3477.
17 L. Qiao, C. Zhang, C.-C. Shu, H. W. T. Morgan, J. E. McGrady and Z.-M. Sun, $[Cu_4@E_{18}]^{4-}$ (E = Sn, Pb): Fused Derivatives of Endohedral Stannaspherene and Plumbaspherene, *J. Am. Chem. Soc.*, 2020, **142**, 13288–13293.
18 Y. Wang, J. E. McGrady and Z.-M. Sun, Solution-Based Group 14 Zintl Anions: New Frontiers and Discoveries, *Acc. Chem. Res.*, 2021, **54**, 1506–1516.
19 H. W. T. Morgan, C.-C. Shu, Z.-M. Sun and J. E. McGrady, Missing Link in the Growth of Lead-Based Zintl Clusters: Isolation of the Dimeric Plumbaspherene $[Cu_4Pb_{22}]^{4-}$, *J. Am. Chem. Soc.*, 2022, **144**, 8007–8017.
20 Y.-H. Xu, W.-J. Tian, A. Muñoz-Castro, G. Frenking and Z.-M. Sun, An all-metal fullerene: $[K@Au_{12}Sb_{20}]^{5-}$, *Science*, 2023, **382**, 840–843.
21 R. J. Wilson, N. Lichtenberger, B. Weinert and S. Dehnen, Intermetalloid and Heterometallic Clusters Combining p-Block (Semi)Metals with d- or f-Block Metals, *Chem. Rev.*, 2019, **119**, 8506–8554.
22 J. E. McGrady, F. Weigend and S. Dehnen, Electronic structure and bonding in endohedral Zintl clusters, *Chem. Soc. Rev.*, 2022, **51**, 628–649.
23 L. Qiao, J. E. McGrady and Z.-M. Sun, in *Comprehensive Inorganic Chemistry III*, ed. J. Reedijk and K. R. Poeppelmeier, 3rd edn, Elsevier, Oxford, 2023, pp. 903–933, DOI: 10.1016/B978-0-12-823144-9.00014-5.
24 W.-J. Tian, Z.-S. Li, S.-D. Li and Z.-M. Sun, in *Comprehensive Computational Chemistry*, ed. M. Yáñez and R. J. Boyd, 1st edn, Elsevier, Oxford, 2024, pp. 452–470, DOI: 10.1016/B978-0-12-821978-2.00078-7.
25 F. Lips, I. Schellenberg, R. Pöttgen and S. Dehnen, The subtle influence of binary versus homoatomic zintl ions: the phenyl-ligated trimetallic cage [Sn(2)Sb(5)(ZnPh)(2)](3-), *Chemistry*, 2009, **15**, 12968–12973.
26 T. F. Fässler and S. D. Hoffmann, Endohedral Zintl Ions: Intermetalloid Clusters, *Angew. Chem., Int. Ed.*, 2004, **43**, 6242–6247.
27 C. Liu, L.-J. Li, X. Jin, J. E. McGrady and Z.-M. Sun, Reactivity Studies of $[Co@Sn_9]^{4-}$ with Transition Metal Reagents: Bottom-Up Synthesis of Ternary Functionalized Zintl Clusters, *Inorg. Chem.*, 2018, **57**, 3025–3034.
28 M. M. Gillett-Kunnath, J. I. Paik, S. M. Jensen, J. D. Taylor and S. C. Sevov, Metal-Centered Deltahedral Zintl Ions: Synthesis of $[Ni@Sn_9]^{4-}$ by Direct Extraction from Intermetallic Precursors and of the Vertex-Fused Dimer $[\{Ni@Sn8(\mu\text{-}Ge)_{1/2}\}_2]^{4-}$, *Inorg. Chem.*, 2011, **50**, 11695–11701.
29 M. J. Frisch, G. W. Trucks, H. B. Schlegel, G. E. Scuseria, M. A. Robb, J. R. Cheeseman, G. Scalmani, V. Barone,

G. A. Petersson, H. Nakatsuji, X. Li, M. Caricato, A. V. Marenich, J. Bloino, B. G. Janesko, R. Gomperts, B. Mennucci, H. P. Hratchian, J. V. Ortiz, A. F. Izmaylov, J. L. Sonnenberg, D. Williams-Young, F. Ding, F. Lipparini, F. Egidi, J. Goings, B. Peng, A. Petrone, T. Henderson, D. Ranasinghe, V. G. Zakrzewski, J. Gao, N. Rega, G. Zheng, W. Liang, M. Hada, M. Ehara, K. Toyota, R. Fukuda, J. Hasegawa, M. Ishida, T. Nakajima, Y. Honda, O. Kitao, H. Nakai, T. Vreven, K. Throssell, J. A. Montgomery Jr., J. E. Peralta, F. Ogliaro, M. J. Bearpark, J. J. Heyd, E. N. Brothers, K. N. Kudin, V. N. Staroverov, T. A. Keith, R. Kobayashi, J. Normand, K. Raghavachari, A. P. Rendell, J. C. Burant, S. S. Iyengar, J. Tomasi, M. Cossi, J. M. Millam, M. Klene, C. Adamo, R. Cammi, J. W. Ochterski, R. L. Martin, K. Morokuma, O. Farkas, J. B. Foresman and D. J. Fox, *Gaussian 16 Rev. B.01.*, 2016.

30 P. V. R. Schleyer, C. Maerker, A. Dransfeld, H. Jiao and N. J. R. van Eikema Hommes, Nucleus-Independent Chemical Shifts: A Simple and Efficient Aromaticity Probe, *J. Am. Chem. Soc.*, 1996, (118), 6317–6318.

31 Z. Chen, C. S. Wannere, C. Corminboeuf, R. Puchta and P. V. R. Schleyer, Nucleus-Independent Chemical Shifts (NICS) as an Aromaticity Criterion, *Chem. Rev.*, 2005, **105**, 3842–3888.

32 S. Klod and E. Kleinpeter, Ab initio calculation of the anisotropy effect of multiple bonds and the ring current effect of arenes—application in conformational and configurational analysis, Journal of the Chemical Society, *Perkin Transact.*, 2001, **2**, 1893–1898, DOI: **10.1039/B009809O**.

33 Z. Liu, T. Lu and Q. Chen, An sp-hybridized all-carboatomic ring, cyclo[18]carbon: Bonding character, electron delocalization, and aromaticity, *Carbon*, 2020, **165**, 468–475.

34 D. Y. Zubarev and A. I. Boldyrev, Developing paradigms of chemical bonding: adaptive natural density partitioning, *Phys. Chem. Chem. Phys.*, 2008, **10**, 5207–5217.

35 C. Adamo and V. Barone, Toward reliable density functional methods without adjustable parameters: The PBE0 model, *J. Chem. Phys.*, 1999, **110**, 6158–6170.

36 F. Weigend and R. Ahlrichs, Balanced basis sets of split valence, triple zeta valence and quadruple zeta valence quality for H to Rn: Design and assessment of accuracy, *Phys. Chem. Chem. Phys.*, 2005, **7**, 3297–3305.

37 F. Weigend, Accurate Coulomb-fitting basis sets for H to Rn, *Phys. Chem. Chem. Phys.*, 2006, **8**, 1057–1065.

38 S. Grimme, J. Antony, S. Ehrlich and H. Krieg, A consistent and accurate ab initio parametrization of density functional dispersion correction (DFT-D) for the 94 elements H-Pu, *J. Chem. Phys.*, 2010, **132**, 154104.

39 T. Yanai, D. P. Tew and N. C. Handy, A new hybrid exchange–correlation functional using the Coulomb-attenuating method (CAM-B3LYP), *Chem. Phys. Lett.*, 2004, **393**, 51–57.

40 A. Tuer, S. Krouglov, R. Cisek, D. Tokarz and V. Barzda, Three-dimensional visualization of the first hyperpolarizability tensor, *J. Comput. Chem.*, 2011, **32**, 1128–1134.

41 T. Lu and F. Chen, Multiwfn: A multifunctional wavefunction analyzer, *J. Comput. Chem.*, 2012, **33**, 580–592.

42 W. Humphrey, A. Dalke and K. Schulten, VMD: Visual molecular dynamics, *J. Mol. Graphics*, 1996, **14**, 33–38.

43 K. Fukui, *Frontier Orbitals and Reaction Paths: Selected Papers of Kenichi Fukui[M]*, World Scientific, Singapore, 1997, pp. 1–300.

44 P. K. Chattaraj, G. H. Liu and R. G. Parr, Chemical reactivity indexes in density functional theory, *J. Comput. Chem.*, 1999, **20**, 129–154.

45 F. Cheng-Cheng, Z. Zhang, W. Zi-Rui, L. De-Jing, L. Qiao-Hong, Z. Lei and Z. Jian, Experimental and Theoretical Studies on Effects of Structural Modification of Tin Nanoclusters for Third-Order Nonlinear Optical Properties, *Inorg. Chem.*, 2021, **60**, 1885–1892.

46 G. Xiang, N. Li, G.-H. Chen, Q.-H. Li, S.-M. Chen, Y.-P. He and J. Zhang, Enhancing Third-Order Nonlinear Optical Property by Regulating Interaction between Zr4(embonate)6 Cage and *N*,*N*-Chelated Transition-Metal Cation, *Molecules*, 2023, **28**, 2301.

47 Z. Wang, Y. Yan, J. Chen, Q.-H. Li and J. Zhang, Designed metal–organic π-clusters combining the aromaticity of the metal cluster and ligands for a third-order nonlinear optical response, *Mater. Horiz.*, 2024, **11**, 297–302.

48 Z. Wang, W. Yan, G. Zhao, K. Wu, Z.-G. Gu, Q.-H. Li and J. Zhang, Novel Third-Order Nonlinear Optical Materials with Craig-Möbius Aromaticity, *J. Phys. Chem. Lett.*, 2021, **12**, 11784–11789.

49 J. Yu, Y. Sun, K. Geng, J. Huang, Y. Cui and H. Hou, Third-Order Nonlinear Optical Modulation Behavior of Photoresponsive Bimetallic MOFs, *Inorg. Chem.*, 2024, **63**, 6526–6536.

50 Z. Liu, T. Lu and Q. Chen, An sp-hybridized all-carboatomic ring, cyclo[18]carbon: Electronic structure, electronic spectrum, and optical nonlinearity, *Carbon*, 2020, **165**, 461–467.

51 Q. Zhou, Y. Guo and Y. Zhu, Photocatalytic sacrificial H2 evolution dominated by micropore-confined exciton transfer in hydrogen-bonded organic frameworks, *Nat. Catal.*, 2023, **6**, 574–584.

52 N. Natarajan, L.-X. Shi, H. Xiao, J.-Y. Wang, L.-Y. Zhang, X. Zhang and Z.-N. Chen, PtAu3 cluster complexes with narrow-band emissions for solution-processed organic light emitting diodes, *J. Mater. Chem. C*, 2019, **7**, 2604–2614.

53 A. D. Becke and K. E. Edgecombe, A simple measure of electron localization in atomic and molecular systems, *J. Chem. Phys.*, 1990, **92**, 5397–5403.

54 A. Savin, A. D. Becke, J. Flad, R. Nesper, H. Preuss and H. G. von Schnering, A New Look at Electron Localization, *Angew. Chem., Int. Ed. Engl.*, 1991, **30**, 409–412.

55 A. Savin, R. Nesper, S. Wengert and T. F. Fässler, ELF: The Electron Localization Function, *Angew. Chem., Int. Ed. Engl.*, 1997, **36**, 1808–1832.